Origin of the High Specific Capacity in Sodium Manganese Hexacyanomanganate br

Kevin Hurlbutt, Feliciano Giustino, George Volonakis, Mauro Pasta

CHEMISTRY OF MATERIALS

pubs.acs.org/cm

Article

Origin of the High Specific Capacity in Sodium Manganese Hexacyanomanganate

Kevin Hurlbutt, Feliciano Giustino, George Volonakis,* and Mauro Pasta*

Cite This: *Chem. Mater.* 2022, 34, 4336−4343

Read Online

ACCESS | Metrics & More | Article Recommendations | Supporting Information

ABSTRACT: Sodium manganese hexacyanomanganate, $Na_xMn[Mn(CN)_6]$, is an electrochemically active Prussian blue analogue (PBA) that has been studied experimentally as an electrode material in rechargeable sodium-ion batteries. It has a reversible specific capacity of 209 mA h g^{-1}, which is substantially higher than the theoretical specific capacity of 172 mA h g^{-1} expected for two reduction events conventional in PBAs. It has been suggested that the high specific capacity originates from this compound's unique ability to insert a third sodium ion per formula unit. However, the plausibility of this mechanism has remained ambiguous. Here, we use density functional theory (DFT) with a hybrid functional to calculate the formation energies of various oxidation states and magnetic phases of the $Na_xMn[Mn(CN)_6]$ system. We confirm that the compound $Na_3Mn^{II}[Mn^{I}(CN)_6]$ is, indeed, thermodynamically stable. It contains manganese(I), and the sodium ions occupy the interfacial position of the lattice subcubes. We also provide strong evidence that the phase of the fully oxidized $Mn[Mn(CN)_6]$ compound is charge-disproportionated, containing manganese(II) and manganese(IV). We proceed to show that the presence of crystalline water increases the reduction potential of the system and that the hydrated compounds have theoretical crystal geometries and reduction potentials that closely match the experiment. This work clarifies the charge-storage mechanism in a well-known but less-understood PBA.

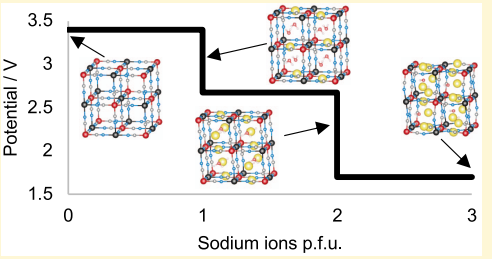

INTRODUCTION

The Prussian blue analogs (PBAs) are a family of electrochemically active compounds with great promise as electrode materials in next-generation batteries.[1,2] They have a wide composition space, and they are capable of reversible electrochemical reactions with diverse metals including sodium,[3] potassium,[4] rubidium,[5] magnesium,[6] aluminum,[7] and others. Depending on their composition, PBAs can insert one or two ions into the interstitial subcube of their open-framework crystal structure.[8] In addition to their technological relevance, PBAs are a useful platform for the study of phenomena in solid-state physics and inorganic chemistry, including charge-transfer-accompanied spin transitions,[9] mixed valency,[10] and defect stability.[11]

Sodium manganese hexacyanomanganate, $Na_xMn[Mn(CN)_6]$, is a PBA of particular interest. In 2014, Pasta and co-workers[12] observed a reversible specific capacity in sodium manganese hexacyanomanganate of 209 mA h g^{-1}. This is 22% higher than the theoretical specific capacity that would be expected from the reversible (de)insertion of two sodium ions per formula unit. Furthermore, they observed three distinct voltage plateaus in the galvanostatic discharge profile. It was hypothesized that the extra capacity came from the insertion of a third sodium ion with the reduction of the carbon-coordinated manganese to manganese(I), as shown in Figure 1. The study included high-quality synchrotron X-ray diffraction (XRD) data, but the authors were unable to refine the structure sufficiently to determine conclusively the positions or number of the sodium ions. Work from Wessells and co-workers in 2018[13] provided good X-ray spectroscopic evidence for the formation of monovalent manganese, supporting the idea that the material inserts three sodium ions.

Here, we investigate the material theoretically using density functional theory (DFT) using a hybrid functional to account for the strong electronic correlation in this material.[14] First, we calculate the formation energies of a pseudobinary mixture of sodium atoms with manganese hexacyanomanganate (empty of any interstitial sodium atoms) to build the convex hull and to determine whether the hypothetical compound $Na_3Mn[Mn(CN)_6]$ is thermodynamically stable. We discuss the crystal structure of the simulated compounds compared to the experiment. We then examine the compounds' electronic structures and oxidation states through their projected densities of states (PDOSs). Finally, we investigate the effect crystalline water has on the stability of the system. We construct the phase diagram of the ground-state composition $Na_xMn[Mn(CN)_6]\cdot wH_2O$ by calculating the system's grand potential. We use this to discuss the effect of crystalline water

Received: December 3, 2021
Revised: April 19, 2022
Published: May 3, 2022

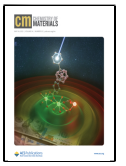

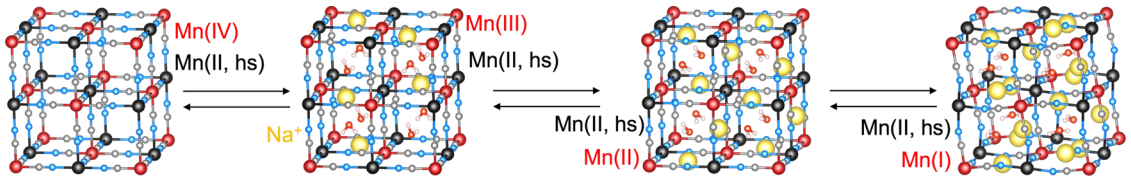

Figure 1. Schematic of the reversible insertion of three sodium ions (per formula unit) into the open-framework $Mn[Mn(CN)_6]$. Darker red atoms are carbon-coordinated manganese, black atoms are nitrogen-coordinated manganese, gray are carbon, light blue are nitrogen, gold are sodium, lighter red are oxygen, and white are hydrogen.

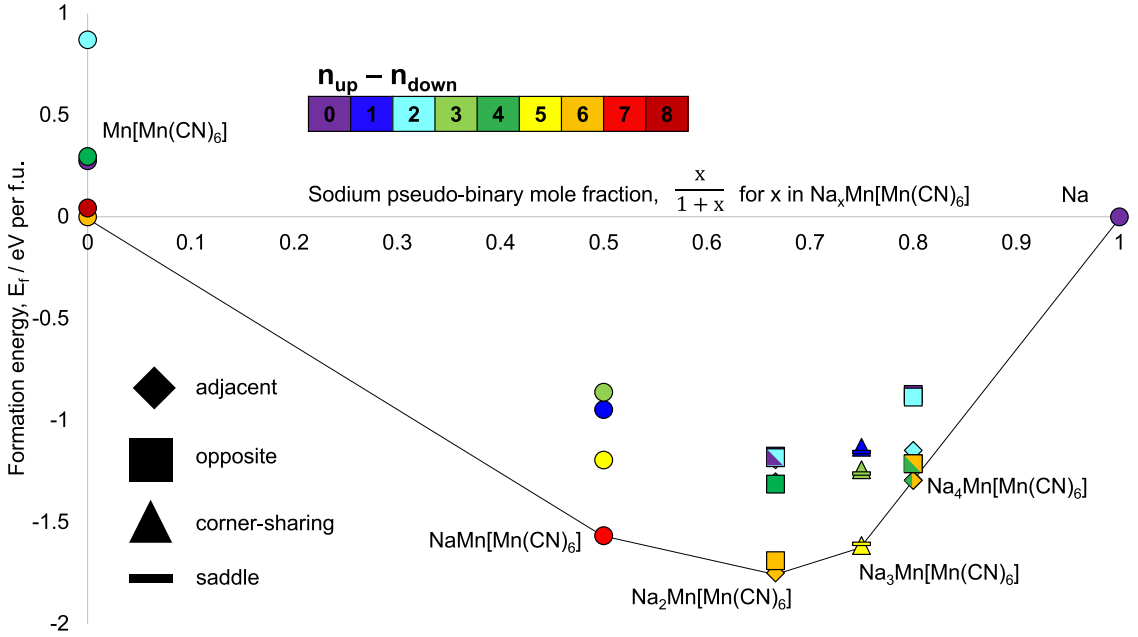

Figure 2. Formation energies for the $Na_xMn[Mn(CN)_6]$ system. The color of the data points signifies the total magnetic moment of the unit cell (in units of the Bohr magneton), which is equal to the difference between the number of majority- and minority-spin electrons. The shapes of the data points are on the left. For the $x = 0$ and 1 phases, there is only one option for the arrangement of sodium ions and their data points are represented with circles. The convex hull is connected by the black line.

on the material's reduction potential versus Na^+/Na. This work is the first thorough, theoretical investigation of one of the most important PBA compositions ever reported because it has the highest-ever reversible specific capacity for sodium ions. We present data on the material's crystal structure and electronic structure that are in excellent agreement with experimental data and that, together, answer conclusively the question of the origin of the high specific capacity in sodium manganese hexacyanomanganate.

RESULTS AND DISCUSSION

Convex Hull of Formation Energies. The formation energy of an inserting electrode material is defined relative to some reference phases. Usual reference phases are the minimal and maximal stoichiometry for the alkali ion. Previous studies, including that of and Goodenough, Henkelman, and co-workers, have considered the formation energies of different PBAs relative to the fully empty lattice (that is, 0 sodium ions per formula unit) and the phase with two sodium ions per formula unit.[15] However, the point of the present study is to determine theoretically the maximal sodium stoichiometry for $Na_xMn[Mn(CN)_6]$. More precisely, the question is whether $Na_3Mn[Mn(CN)_6]$ is stable against separation into $Na_2Mn[Mn(CN)_6]$ and sodium metal. The appropriate reference phases then are the empty manganese hexacyanomanganate lattice and sodium metal.

The formation energy of a pseudobinary mixture of sodium atoms with the empty manganese hexacyanomanganate lattice (that is, the lattice containing no inserted sodium atoms) is

$$E_f(x) = \frac{E(Na_xMn[Mn(CN)_6]) - E(Mn[Mn(CN)_6]) - xE(Na)}{1 + x}$$

in which x is the number of sodium atoms per formula unit.[16] The total energy also depends strongly on the unit cell's magnetic moment. For each value of x, various electronic configurations are plausible depending on the manganese ions' oxidation states, spin configurations (that is low spin versus high spin), and spin alignment. The formation energies for the phases including the different magnetic configurations are shown in Figure 2.

For the fully oxidized compound, $Mn[Mn(CN)_6]$, the two magnetic phases, 6 and 8 μ_B, where μ_B is the Bohr magneton, are essentially degenerate. As discussed in the next section, the two phases have very different crystal structures, and only the 8 μ_B phase is in excellent agreement with the experiment. For the compound $NaMn[Mn(CN)_6]$, the ground-state magnetization is 7 μ_B and is well separated in energy from the other magnetic phases. The compound $Na_2Mn[Mn(CN)_6]$ has a ground-state

https://doi.org/10.1021/acs.chemmater.1c04167
Chem. Mater. 2022, 34, 4336−4343

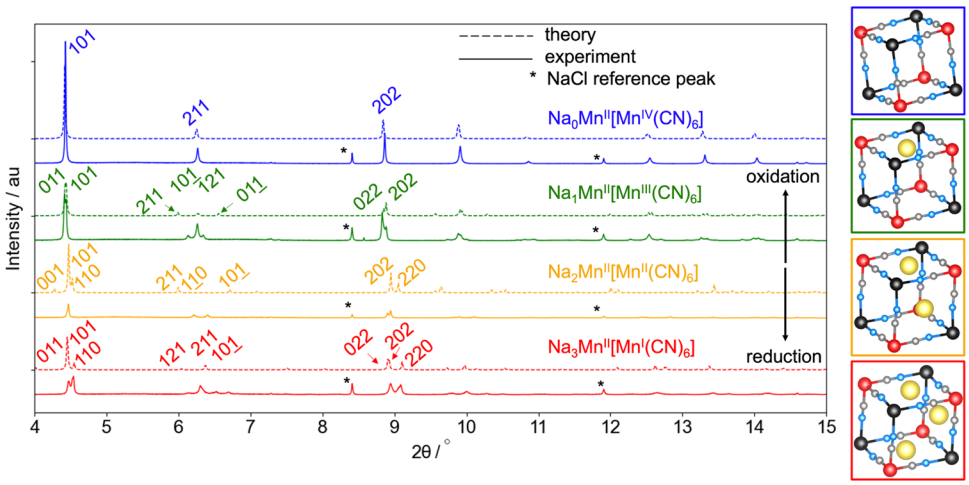

Figure 3. Crystal structures and simulated diffractograms. The simulated (dashed line) and experimental (solid line, collected by Pasta and co-workers[12] at room temperature) patterns are plotted for the four compounds $Mn[Mn(CN)_6]$, $NaMn[Mn(CN)_6]$, $Na_2Mn[Mn(CN)_6]$, and $Na_3Mn[Mn(CN)_6]$. Peak indices are included for the simulated patterns and the asterisk indicates sodium chloride reference peaks in the experimental data. The corresponding crystal structures are shown at right.

magnetization of 6 μ_B. The ground-state magnetization for the compound $Na_3Mn[Mn(CN)_6]$ is 5 μ_B. For $Na_4Mn[Mn(CN)_6]$, the two magnetic phases μ = 6 and 4 μ_B are degenerate.

The sodium ions reside in the faces separating two subcubes. (The subcube vertices are eight manganese ions and the edges are cyanide ligands.) For the compound $Na_2Mn[Mn(CN)_6]$, there are two arrangements of the sodium ions that are local minima on the potential energy surface. In one arrangement, the sodium ions occupy faces that share an edge, referred in Figure 2 as "adjacent" (see Figure SI.1). In the other arrangement, sodium ions occupy subcube faces opposite each other, referred to here as "opposite." The edge-sharing phase is just 11 meV atom^{-1} lower in energy. For $Na_3Mn[Mn(CN)_6]$, there are also two possible sodium-ion arrangements. The three ions can occupy either three faces of the interstitial subcube that share a corner or three faces in a "saddle" arrangement. These two phases are essentially degenerate in energy (the corner-sharing arrangement is 2 meV atom^{-1} lower in energy). In the two sodium-ion arrangements for $Na_4Mn[Mn(CN)_6]$, the faces that do not contain a sodium ion are either edge sharing or opposite. The adjacent arrangement is the ground state.

The convex hull of formation energies is, geometrically, the unique, minimal set containing all of the formation energies. The convex hull is the phases $Mn[Mn(CN)_6]$, $NaMn[Mn(CN)_6]$, $Na_2Mn[Mn(CN)_6]$, $Na_3Mn[Mn(CN)_6]$, and sodium metal. Physically, the convex hull of formation energies defines the stable phases. For any meta-stable phase with a formation energy above the convex hull, the system's total energy will decrease on transformation into phases whose formation energies do lie on the convex hull. Since $Na_3Mn[Mn(CN)_6]$ is part of the convex hull, the experimental observation of the insertion of three sodium ions into the lattice is, indeed, thermodynamically reasonable.

Figure 2 indicates that $Na_3Mn[Mn(CN)_6]$ is stable against separation into $Na_2Mn[Mn(CN)_6]$ and sodium metal. More generally, each of the compounds $Na_xMn[Mn(CN)_6]$ (for $x \in$ 0, 1, 2, 3) is stable against separation into any of the other oxidation states studied here. The phase with three sodium ions per formula unit, x = 3, is not stable in PBAs generally. This is, to the authors' knowledge, the first PBA to be shown to be stable with three sodium ions per formula unit. We note that this is one slice of the higher-dimensional set of formation energies. It is conceivable that the compound could break down into other chemical species like sodium cyanide. However, other decomposition pathways at room temperature are unlikely. First, the sample from Pasta and co-workers was cycled reversibly and stable enough to collect the XRD data discussed in the next section. Second, the low-potential behavior of a closely related composition, sodium manganese hexacyanochromate ($Na_xMn[Cr(CN)_6]$), has previously been explored experimentally.[17] The lattice was found to be stable below the minimum potential (about 1.21 V versus Na^+/Na) that these calculations predict is necessary to insert the third sodium ion. Third, closely related PBA compositions have been found to be thermally stable up to 200 °C or higher.[18] Interestingly, $Na_4Mn[Mn(CN)_6]$ lies almost exactly on the convex hull. This indicates that the insertion of a fourth sodium ion may be possible. However, it is essentially degenerate with the phase-separated mixture of sodium metal with $Na_3Mn[Mn(CN)_6]$, so experimental observation would be challenging (see Figure SI.2).

Crystal Structures and Sodium-Ion Positions. The crystal structures and simulated X-ray diffractograms for the four oxidation states are shown in Figure 3 along with the experimental synchrotron XRD data collected by Pasta and co-workers.[12] For the fully oxidized $Mn[Mn(CN)_6]$, the diffraction pattern for the μ = 8 μ_B phase is shown. This phase is face-centered cubic (space group $Fm\bar{3}m$) with a lattice parameter of 10.7 Å. The most intense peak arises from the (101) reflection at 4.42°. It is clear that the computed cubic crystal structure for μ = 8 μ_B is in excellent agreement with synchrotron XRD data. The μ = 6 μ_B phase for this compound has a tetragonal crystal geometry with lattice parameters a = 10.2 Å and c/a = 1.06. The crystal structure and simulated XRD pattern are shown in Figure SI.3. The calculated energetic difference between the 6 and the 8 μ_B phases, computed at absolute zero temperature, is only 3 meV atom^{-1}. So while it is entirely reasonable that the ground state at finite temperature is observed to have the crystal structure consistent with the 8 μ_B phase, it is beyond the capability of DFT to

https://doi.org/10.1021/acs.chemmater.1c04167
Chem. Mater. 2022, 34, 4336−4343

Table 1. Comparison of Experimental and Computational Lattice Parameters

	experimental		computational		
	a (Å)	$b = c$ (Å)	a (Å)	b (Å)	c (Å)
$Mn[Mn(CN)_6]$	10.706		10.736	10.732	
$NaMn[Mn(CN)_6]$	10.688	10.750	10.728	10.726	
$Na_2Mn[Mn(CN)_6]$	10.658	10.616	10.607	10.703	
$Na_3Mn[Mn(CN)_6]$	10.459	10.905	10.710	10.633	10.475

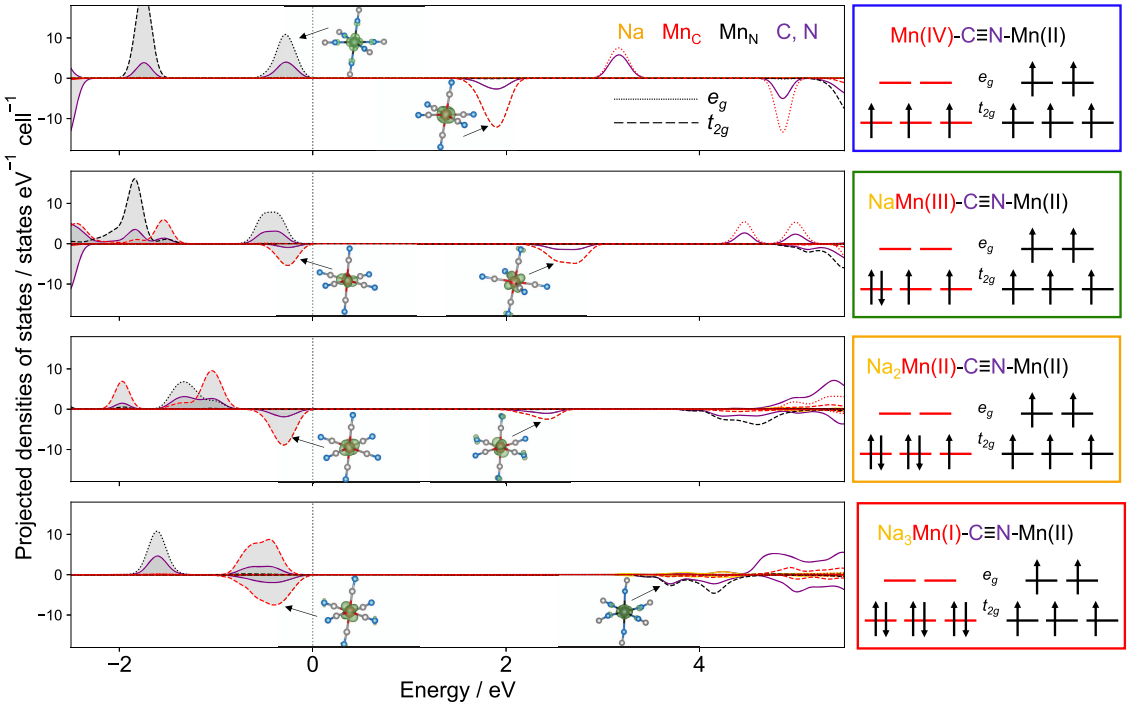

Figure 4. Projected densities of states (PDOSs), band-decomposed charge densities, and electronic configurations. Plots and configurations correspond to 0, 1, 2, and 3 sodium ions per formula unit from top to bottom. In the PDOSs, red, black, purple, and gold lines refer to states arising from orbitals on the carbon-coordinated manganese, nitrogen-coordinated manganese, cyanide ligands, and sodium, respectively. Solid, dashed, and dotted lines refer to states arising from (s and p), t_{2g}, and e_g orbitals, respectively. The charge-density isosurfaces are for the valence-band and conduction-band states, drawn at 0.01 e Å^{-3}.

discern between the two phases. Future study explicitly including thermal excitation is needed.

In the simulated pattern for the compound $NaMn[Mn(CN)_6]$, the most intense peaks arise from the (011) and (110) reflections at 4.42 and 4.44°, respectively. This, too, is in excellent agreement with the synchrotron XRD data. The splitting of these peaks is indicative of the breaking of the cubic symmetry in the more oxidized phase.

The simulated pattern for $Na_2Mn[Mn(CN)_6]$ is also very similar to the experiment. The two peaks caused by the (101) and (110) reflections are aligned with two experimental peaks centered at about 4.45 and 4.47°. (Note that the (001) reflection at 4.27° in the simulated pattern results from long-range ordering of sodium ions due to the model's periodic boundary conditions. Figure SI.4 shows the pattern simulated without sodium ions.)

For $Na_3Mn[Mn(CN)_6]$, the simulated data also generally match the empirical data well. The model has three reflections, (011), (101), and (110), which match three experimental peaks at 4.47, 4.52, and 4.54°.

Table 1 lists the experimental lattice parameters versus the calculated values. The values are for a "cubic equivalent" cell and refer to the distance between nearest-neighbor carbon-coordinated manganese ions. The values from the theory are extremely close to those from the experiment. The validation of the model warrants the following closer study of the electronic structure.

Finally, from Figure 2, it is clear that the energetic separations between the possible arrangements of sodium ions are small (especially compared to the effect of spin state), on the order of thermal excitation at 300 K. So, while DFT calculations are performed at absolute zero temperature, appreciable disorder in the sodium ions' positions is to be expected at room temperature. This disorder from thermal excitation likely contributes substantially to the differences between the theoretical and experimental diffractograms (especially at degrees 2θ above 6°), as well as the lattice parameters because those data were collected at room temperature.

Electronic Structures and Oxidation States. The projected densities of states (PDOSs) and electronic configurations that are calculated using the atom-projected magnetic moments for the four compounds are shown in Figure 4. The figure also shows the valence- and conduction-band-decomposed charge densities. All of these states arise from highly localized manganese orbitals.

https://doi.org/10.1021/acs.chemmater.1c04167
Chem. Mater. 2022, 34, 4336−4343

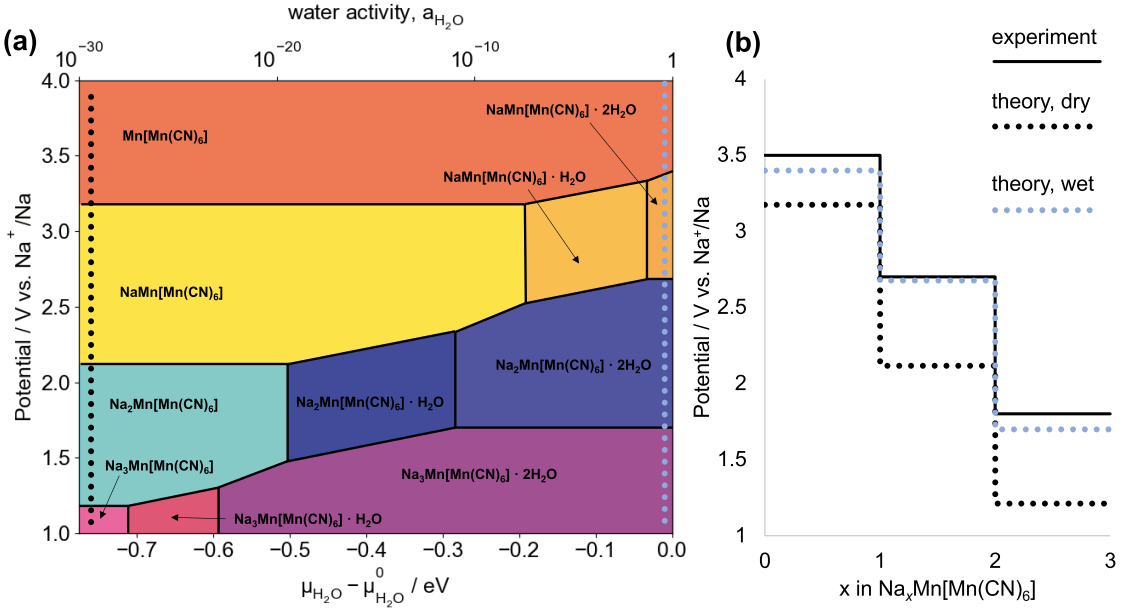

Figure 5. Phase diagram and simulated galvanostatic curve. In panel (a), the stable phase of the $Na_xMn[Mn(CN)_6]\cdot wH_2O$ system is plotted as a function of voltage and chemical potential of water at 300 K. In panel (b), the simulated galvanostatic discharge curves are plotted for a drier electrolyte (lower chemical potential for water) (black dotted line) and for a wetter electrolyte (higher chemical potential for water) (blue dotted line). The average experimental potential is plotted from Pasta and co-workers[12] for comparison.

For the fully oxidized compound, $Mn[Mn(CN)_6]$, the $\mu = 8$ μ_B phase has atom-projected magnetic moments of $\mu_{Mn_C} = 3.023$ μ_B and $\mu_{Mn_N} = 4.567$ μ_B. This is consistent with an electronic configuration of $(Mn_C(t_{2g}^3), Mn_N(t_{2g}^3e_g^2))$. In this phase, the nitrogen-coordinated manganese is high spin and the two manganese ions are spin-aligned. The two manganese ions are in oxidation states $(Mn_C(IV), Mn_N(II))$, so this phase is charge-disproportionated. This is an agreement with experiment.[19] The PDOS shows that the conduction-band states arise from spin-down, t_{2g} orbitals on the carbon-coordinated manganese. The electronic configuration for the nearly degenerate $\mu = 6$ μ_B is $(Mn_C(t_{2g}^4), Mn_N(t_{2g}^3e_g^1))$. This oxidation state $(Mn_C(III), Mn_N(III))$ has a singly occupied e_g orbital, which gives rise to a Jahn−Teller distortion and the tetragonal geometry discussed above.

On reduction to the compound $NaMn[Mn(CN)_6]$, the spin-down, carbon-coordinated t_{2g} orbitals become partially occupied; both the valence and conduction bands arise from spin-down, t_{2g} orbitals on the carbon-coordinated manganese. The atom-projected magnetic moments for this $\mu = 7$ μ_B phase are $\mu_{Mn_C} = 2.013$ μ_B and $\mu_{Mn_N} = 4.572$ μ_B; the orbital occupations are $(Mn_C(t_{2g}^4), Mn_N(t_{2g}^3e_g^2))$. In this phase, the nitrogen-coordinated carbon remains high spin and the two manganese ions are spin-aligned.

A further reduction to the compound $Na_2Mn[Mn(CN)_6]$ adds an electron to the spin-down, carbon-coordinated-manganese t_{2g} orbital, resulting in increased density of states in the valence band arising from these orbitals. The conduction band still originates from these same, carbon-coordinated-manganese, spin-down t_{2g} orbitals (albeit with lower density of states). The atom-projected magnetic moments are $\mu_{Mn_C} = 1.075$ μ_B and $\mu_{Mn_N} = 4.567$ μ_B and the electronic configuration is $(Mn_C(t_{2g}^5), Mn_N(t_{2g}^3e_g^2))$. The nitrogen-coordinated manganese is still high spin, and the manganese ions are still spin-aligned.

Reduction to $Na_3Mn[Mn(CN)_6]$ fully occupies the t_{2g} orbitals on the carbon-coordinated manganese, so the valence band arises from these orbitals. The atom-projected magnetic moments are $\mu_{Mn_C} = 0.094$ μ_B and $\mu_{Mn_N} = 4.561$ μ_B. This implies an orbital occupation of $(Mn_C(t_{2g}^6), Mn_N(t_{2g}^3e_g^2))$ with high-spin nitrogen-coordinated manganese.

The theoretical compound $Na_4Mn[Mn(CN)_6]$ would be naively expected to attain an oxidation state of either $(Mn_C(I), Mn_N(I))$ or perhaps even $(Mn_C(0), Mn_N(II))$. However, the atom-projected magnetic moments on the two manganese ions are equal to those in the $Na_3Mn^{II}[Mn^{I}(CN)_6]$ system. As Figure SI.5 shows, the valence-band states arise from sodium orbitals. The only difference between the degenerate 4 and 6 μ_B phases is the spin of the electron on the sodium atom; the electronic structures of the lattice ions are identical in the two magnetic phases.

Overall, the high specific capacity in sodium manganese hexacyanomanganate originates, in part, from the fact that $Na_2Mn[Mn(CN)_6]$ has a relatively low-energy conduction-band state arising from an unoccupied t_{2g} orbital on the carbon-coordinated manganese. Reduction to $Na_3Mn[Mn(CN)_6]$ results in the particularly stable electronic configuration $(Mn_C(t_{2g}^6), Mn_N(t_{2g}^3e_g^2))$. The nitrogen-coordinated manganese ion remains manganese(II) over the course of three reduction events from $Mn[Mn(CN)_6]$ to $Na_3Mn[Mn(CN)_6]$. The carbon-coordinated manganese is the exclusive redox center in this system, changing the oxidation state from +4 to +3 to +2 to +1. Furthermore, the nitrogen-coordinated manganese is always high spin, and the two manganese ions are always ferromagnetically aligned. (Though in $Na_3Mn^{II}[Mn^{I}(CN)_6]$, the carbon-coordinated manganese ion's magnetic moment is 0.)

Effect of Crystalline Water. The grand potential governs the phase stability of the compositions $Na_xMn[Mn(CN)_6]\cdot wH_2O$ for various values of x and w. The grand potential for hydrated PBAs was developed by Ong and co-workers[20]

https://doi.org/10.1021/acs.chemmater.1c04167
Chem. Mater. 2022, 34, 4336−4343

following a general treatment of water in intercalation electrodes by Ceder and co-workers.[21] The grand potential is given by

$$\Phi = G(\mathrm{Na}_x\mathrm{Mn[Mn(CN)_6]}\cdot w\mathrm{H_2O}) - x\mu_{\mathrm{Na}} - w\mu_{\mathrm{H_2O}}$$

in which $G(\mathrm{Na}_x\mathrm{Mn[Mn(CN)_6]})$ is the Gibbs energy (approximated by the DFT free energy), μ_{Na} is the chemical potential of sodium particles, and $\mu_{\mathrm{H_2O}}$ is the chemical potential of water particles. An exact treatment of the chemical potential would require including various entropic contributions, including vibrational and configurational excitations of the crystal structures. Here, we make the simplifying assumption that the entropy of the reaction between any two hydrated phases is dominated by the entropy change associated with liquid-phase water entering (or leaving) the crystal.[21−23] So the effect of finite temperature is encapsulated by the chemical potential of the water.

The chemical potential of water, $\mu_{\mathrm{H_2O}}$, can be expressed as

$$\mu_{\mathrm{H_2O}} = \mu^0_{\mathrm{H_2O}} + k_{\mathrm{B}}T\ln(a_{\mathrm{H_2O}})$$

in which $\mu^0_{\mathrm{H_2O}}$ is the reference chemical potential for water and $a_{\mathrm{H_2O}}$ is the activity of water in a liquid electrolyte. The sodium chemical potential is related to the electric potential (or voltage), V, by

$$V = -\frac{\mu_{\mathrm{Na}} - \mu^0_{\mathrm{Na}}}{e}$$

where μ^0_{Na} is the reference chemical potential of sodium metal and e is the fundamental charge.

To calculate the energies of monohydrate and dihydrate phases, water molecules were explicitly included in the crystal structure and full relaxation of lattice vectors and atom positions was performed using the Heyd−Scuseria−Ernzerhof (HSE) functional. The phase diagram that results for the $\mathrm{Na}_x\mathrm{Mn[Mn(CN)_6]}\cdot w\mathrm{H_2O}$ system is shown in Figure 5a. At the lowest chemical potential for water (that is, for the driest electrolyte), the dehydrated ($w = 0$) phase is most stable for all four oxidation states ($x = 0$−3). At the highest chemical potential for water (that is, the wettest electrolyte), the most stable phase has two water molecules per formula unit for x = 1, 2, and 3. For the $x = 0$ compound, though, the dehydrated compound remains the most stable, and neither $\mathrm{Mn[Mn(CN)_6]}\cdot\mathrm{H_2O}$ nor $\mathrm{Mn[Mn(CN)_6]}\cdot 2\mathrm{H_2O}$ appears in the phase diagram. The intermediate hydration states, $\mathrm{NaMn[Mn(CN)_6]}\cdot\mathrm{H_2O}$, $\mathrm{Na_2Mn[Mn(CN)_6]}\cdot\mathrm{H_2O}$, and $\mathrm{Na_3Mn[Mn(CN)_6]}\cdot\mathrm{H_2O}$, are the ground state at intermediate water chemical potentials.

Water has the effect of increasing the reduction potential in closely related PBA compositions,[20] and it also increases the reduction potential of this $\mathrm{Na}_x\mathrm{Mn[Mn(CN)_6]}\cdot w\mathrm{H_2O}$ system, as shown in Figure 5b. The calculated reduction potential for the $\mathrm{Mn^{II}[Mn^{III/IV}(CN)_6]}$couple is 3.17 V versus $\mathrm{Na^+/Na}$; this underestimates the observed average potential of about 3.5 V by 330 mV. $\mathrm{Mn^{II}[Mn^{III/II}(CN)_6]}$ has a calculated reduction potential of 2.12 V versus $\mathrm{Na^+/Na}$, which is 580 mV below the observed average value of about 2.7 V. Finally, the $\mathrm{Mn^{II}[Mn^{II/I}(CN)_6]}$ couple is computationally at 1.21 V versus $\mathrm{Na^+/Na}$, while the average experimental data is around 1.8 V or 590 mV higher. However, the reduction potentials for the hydrated materials at higher chemical potential are 3.4, 2.7, and 1.7 V versus $\mathrm{Na^+/Na}$. These are in much better agreement with the experiment, underestimating observed values by 100, 0, and 100 mV. Figure SI.6 shows that the crystal structures of the hydrated compounds agree with the experiment as well as or better than the structures in Figure 3.

In terms of the electronic structure of the hydrated compounds, electronic states arising from water molecules have energies well below the Fermi level. The states arising from lattice ions and sodium ions are largely unaffected. For all of the compounds, the valence and conduction bands arise from the same orbitals as in the fully dehydrated compounds. The PDOS for the hydrated compounds is shown in Figure SI.7.

CONCLUSIONS

DFT calculations with a hybrid functional reveal that the high specific capacity in sodium manganese hexacyanomanganate arises from the insertion of a third sodium ion into the formula unit, forming $\mathrm{Na_3Mn^{I}[Mn^{II}(CN)_6]}$. All three sodium ions occupy different faces of the interstitial subcube. This compound lies on the convex full of formation energies for this system on account of the particularly stable electronic configuration ($\mathrm{Mn_C}(t_{2g}^6)$, $\mathrm{Mn_N}(t_{2g}^3e_g^2)$). This compound includes the somewhat rare manganese(I) species. The hydrated form of the compound, $\mathrm{Na_3Mn^{I}[Mn^{II}(CN)_6]}\cdot 2\mathrm{H_2O}$, is also stable at high chemical potential for liquid water. Hydration of these materials increases the reduction potential versus $\mathrm{Na^+/Na}$.

One question that remains is why the experimental specific capacity, 209 mA h $\mathrm{g^{-1}}$, while higher than the capacity expected for the (de)insertion of two sodium ions, is still lower than the theoretical value for the (de)insertion of three sodium ions. For the reported composition $\mathrm{Na_{1.96}Mn[Mn(CN)_6]_{1.96}}\cdot 2\mathrm{H_2O}$, the theoretical specific capacity for (de)insertion of three sodium ions is 229 mA h $\mathrm{g^{-1}}$, a difference of 9%. The physiochemical characterization of the as-synthesized material and the good agreement between theory and experiment seems to exclude the presence of hexacyanometallate vacancies as a justification for this discrepancy. A more plausible explanation is that the specific capacity is limited by the electrode's kinetics. Komaba and co-workers reported the beneficial effect of vacancies on K-ion conduction in potassium manganese hexacyanoferrate, highlighting the limited diffusivity in the vacancy-free material.[24] Future theoretical work can examine the activation energy for ion movement through the lattice using, for instance, the nudged-elastic-band method. This work provides a convincing explanation for the origin of the highest-ever observed reversible specific capacity in a PBA and is an important contribution to the theory of PBA electrodes.

METHODS

We performed all DFT calculations using the Vienna ab initio Simulation Package (VASP).[25,26] For all compounds, the atom positions and lattice vectors were relaxed by variable-cell optimization using first the Perdew−Burke−Ernzerhof (PBE) functional[27] and then with the nonlocal, hybrid Heyd−Scuseria−Ernzerhof (HSE) functional.[28] For the HSE functional, we used a screening parameter of 0.2 $\mathrm{Å^{-1}}$ and a mixing of 25% Fock exchange with 75% PBE exchange. The convergence criterion for the electronic steps was a change of less than 10^{-5} eV in the total energy between steps. The convergence criterion for the ionic steps was that the forces on every ion were less than 0.05 eV $\mathrm{Å^{-1}}$. We used a Γ-centered 4 × 4 × 4 **k**-point grid and a plane-wave kinetic-energy cutoff of 520 eV. All calculations were (collinear) spin-polarized; the total magnetization per formula unit was fixed and held constant during relaxation. The structures and total

https://doi.org/10.1021/acs.chemmater.1c04167
Chem. Mater. 2022, 34, 4336−4343

energies were then compared between different values for the magnetization. For the structures that contain water, water molecules were included explicitly in the model and full relaxation of the lattice vectors and atom positions (including water) were performed again using the HSE functional. Water molecules were placed in subcubes with sodium ions; the lower-energy configuration is the migration of the sodium ions to the subcube faces and the migration of the water molecules to the centers of the subcubes. In calculating the formation energies, the reference energy for $Mn[Mn(CN)_6]$ was the energy of the 6 μ_B phase. The reference chemical potential of water in Figure 5 is −17.9 eV, the value that best reproduces both the experimental galvanostatic and crystallographic data. This value can alternatively be calculated using a method described by Nørskov and co-workers.[29] The chemical potential of a water molecule is calculated at 0.035 bar and 300 K because, at this temperature and pressure, gas- and liquid-phase water are in equilibrium. The DFT total energy is computed and combined with empirical thermodynamic data. Using this method with the HSE06 functional and data from the NIST-JANAF database, the calculated chemical potential is −18.0 eV; this is 0.1 eV below (or 0.56% of) the value that best reproduces the experimental data. The X-ray diffraction reflections were calculated using an incident photon wavelength of λ = 0.413737 Å in VESTA, and diffractograms were simulated using a Lorentzian function with γ = 0.01°.

■ ASSOCIATED CONTENT

Supporting Information

The Supporting Information is available free of charge at https://pubs.acs.org/doi/10.1021/acs.chemmater.1c04167.

Additional computational details including PDOS for the hydrated phases; PDOS for the phase with four sodium ions per formula unit; detailed diffractograms; ion-arrangement diagram; and a phase diagram (PDF)

■ AUTHOR INFORMATION

Corresponding Authors

George Volonakis − *Univ Rennes, ENSCR, INSA Rennes, CNRS, ISCR (Institut des Sciences Chimiques de Rennes), UMR 6226, Rennes F-35000, France;* orcid.org/0000-0003-3047-2298; Email: yorgos.volonakis@univ-rennes1.fr

Mauro Pasta − *Department of Materials, University of Oxford, Oxford OX1 3PH, United Kingdom;* orcid.org/0000-0002-2613-4555; Email: mauro.pasta@materials.ox.ac.uk

Authors

Kevin Hurlbutt − *Department of Materials, University of Oxford, Oxford OX1 3PH, United Kingdom;* orcid.org/0000-0001-7494-0044

Feliciano Giustino − *Oden Institute for Computational Engineering and Sciences and Department of Physics, The University of Texas at Austin, Austin, Texas 78712, United States*

Complete contact information is available at: https://pubs.acs.org/10.1021/acs.chemmater.1c04167

Notes

The authors declare no competing financial interest.

■ ACKNOWLEDGMENTS

The authors gratefully acknowledge the use of the following computer resources: the University of Oxford Advanced Research Computing (ARC) facility (http://dx.doi.org/10.5281/zenodo.22558) and PRACE for awarding time on Beskow based in Sweden at KTH and on ARCHER in the United Kingdom (http://www.archer.ac.uk) through projects 16DECI0064 and 17DECI0090. K.H. and M.P. would like to acknowledge the financial support of the ISCF Faraday Challenge project SOLBAT grant number FIRG026.

■ REFERENCES

(1) Qian, J.; Wu, C.; Cao, Y.; Ma, Z.-F.; Huang, Y.; Ai, X.; Yang, H. Prussian Blue Cathode Materials for Sodium-Ion Batteries and Other Ion Batteries. *Adv. Energy Mater.* **2018**, *8*, No. 1702619.

(2) Wang, L.; Lu, Y.; Liu, J.; Xu, M.; Cheng, J.; Zhang, D.; Goodenough, J. B. A Superior Low-Cost Cathode for a Na-Ion Battery. *Angew. Chem., Int. Ed.* **2013**, *52*, 1964−1967.

(3) Song, J.; Wang, L.; Lu, Y.; Liu, J.; Guo, B.; Xiao, P.; Lee, J. J.; Yang, X. Q.; Henkelman, G.; Goodenough, J. B. Removal of interstitial H2O in hexacyanometallates for a superior cathode of a sodium-ion battery. *J. Am. Chem. Soc.* **2015**, *137*, 2658−2664.

(4) Fiore, M.; Wheeler, S.; Hurlbutt, K.; Capone, I.; Fawdon, J.; Ruffo, R.; Pasta, M. Paving the Way Toward Highly Efficient High-Energy Potassium-Ion Batteries with Ionic-Liquid Electrolytes. *Chem. Mater.* **2020**, *32*, 7653−7661.

(5) Lee, H.-w.; Pasta, M.; Wang, R. Y.; et al. Effect of the alkali insertion ion on the electrochemical properties of nickel hexacyanoferrate electrodes. *Faraday Discuss.* **2014**, *176*, 69−81.

(6) Wang, R. Y.; Wessells, C. D.; Huggins, R. A.; Cui, Y. Highly reversible open framework nanoscale electrodes for divalent ion batteries. *Nano Lett.* **2013**, *13*, 5748−5752.

(7) Reed, L. D.; Ortiz, S. N.; Xiong, M.; Menke, E. J. A rechargeable aluminum-ion battery utilizing a copper hexacyanoferrate cathode in an organic electrolyte. *Chem. Commun.* **2015**, *51*, 14397−14400.

(8) Hurlbutt, K.; Wheeler, S.; Capone, I.; Pasta, M. Prussian Blue Analogs as Battery Materials. *Joule* **2018**, *2*, 1950−1960.

(9) Cammarata, M.; Zerdane, S.; Balducci, L.; Azzolina, G.; Mazerat, S.; Exertier, C.; Trabuco, M.; Levantino, M.; Alonso-Mori, R.; Glownia, J. M.; Song, S.; Catala, L.; Mallah, T.; Matar, S. F.; Collet, E. Charge transfer driven by ultrafast spin transition in a CoFe Prussian blue analogue. *Nat. Chem.* **2021**, *13*, 10−14.

(10) Wojdeł, J. C.; De PR Moreira, I.; Bromley, S. T.; Illas, F. On the prediction of the crystal and electronic structure of mixed-valence materials by periodic density functional calculations: The case of Prussian Blue. *J. Chem. Phys.* **2008**, *128*, No. 044713.

(11) Cattermull, J.; Wheeler, S.; Hurlbutt, K.; Pasta, M.; Goodwin, A. L. Filling vacancies in a Prussian blue analogue using mechanochemical post-synthetic modification. *Chem. Commun.* **2020**, *56*, 7873−7876.

(12) Lee, H.-W.; Wang, R. Y.; Pasta, M.; Woo Lee, S.; Liu, N.; Cui, Y. Manganese hexacyanomanganate open framework as a high-capacity positive electrode material for sodium-ion batteries. *Nat. Commun.* **2014**, *5*, No. 5280.

(13) Firouzi, A.; Qiao, R.; Motallebi, S.; Valencia, C. W.; Israel, H. S.; Fujimoto, M.; Wray, L. A.; Chuang, Y.-D.; Yang, W.; Wessells, C. D. Monovalent manganese based anodes and co-solvent electrolyte for stable low-cost high-rate sodium-ion batteries. *Nat. Commun.* **2018**, *9*, No. 861.

(14) Hurlbutt, K.; Giustino, F.; Pasta, M.; Volonakis, G. Electronic structure and electron-transport properties of three metal hexacyanoferrates. *Chem. Mater.* **2021**, *33*, 7067−7074.

(15) Xiao, P.; Song, J.; Wang, L.; Goodenough, J. B.; Henkelman, G. Theoretical study of the structural evolution of a $Na_2FeMn(CN)_6$ cathode upon Na intercalation. *Chem. Mater.* **2015**, *27*, 3763−3768.

(16) Mayo, M.; Griffith, K. J.; Pickard, C. J.; Morris, A. J. Ab Initio Study of Phosphorus Anodes for Lithium- and Sodium-Ion Batteries. *Chem. Mater.* **2016**, *28*, 2011−2021.

(17) Wheeler, S.; Capone, I.; Day, S.; Tang, C.; Pasta, M. Low-potential Prussian blue analogues for sodium-ion batteries: manganese hexacyanochromate. *Chem. Mater.* **2019**, *31*, 2619−2626.

(18) Parajuli, D.; Tanaka, H.; Sakurai, K.; Hakuta, Y.; Kawamoto, T. Thermal decomposition behavior of prussian blue in various conditions. *Materials* **2021**, *14*, No. 1151.

(19) Klenze, R.; Kanellakopulos, B.; Trageser, G.; Eysel, H. H. Manganese hexacyanomanganate: Magnetic interactions via cyanide in a mixed valence Prussian blue type compound. *J. Chem. Phys.* **1980**, *72*, 5819−5828.
(20) Guo, X.; Wang, Z.; Deng, Z.; Li, X.; Wang, B.; Chen, X.; Ong, S. P. Water Contributes to Higher Energy Density and Cycling Stability of Prussian Blue Analogue Cathodes for Aqueous Sodium-Ion Batteries. *Chem. Mater.* **2019**, *31*, 5933−5942.
(21) Sai Gautam, G.; Canepa, P.; Richards, W. D.; Malik, R.; Ceder, G. Role of Structural H_2O in Intercalation Electrodes: the Case of Mg in Nanocrystalline Xerogel-V_2O_5. *Nano Lett.* **2016**, *16*, 2426−2431.
(22) Ong, S. P.; Wang, L.; Kang, B.; Ceder, G. Li-Fe-P-O_2 phase diagram from first principles calculations. *Chem. Mater.* **2008**, *20*, 1798−1807.
(23) Kirklin, S.; Meredig, B.; Wolverton, C. High-throughput computational screening of new Li-ion battery anode materials. *Adv. Energy Mater.* **2013**, *3*, 252−262.
(24) Hosaka, T.; Fukabori, T.; Kojima, H.; Kubota, K.; Komaba, S. Effect of Particle Size and Anion Vacancy on Electrochemical Potassium Ion Insertion into Potassium Manganese Hexacyanoferrates. *ChemSusChem* **2021**, *14*, 1166−1175.
(25) Kresse, G.; Furthmüller, J.; Hafner, J. Theory of the crystal structures of selenium and tellurium: The effect of generalized-gradient corrections to the local-density approximation. *Phys. Rev. B* **1994**, *50*, 13181−13185.
(26) Kresse, G.; Furthmüller, J. Efficiency of ab-initio total energy calculations for metals and semiconductors using a plane-wave basis set. *Comput. Mater. Sci.* **1996**, *6*, 15−50.
(27) Perdew, J. P.; Burke, K.; Ernzerhof, M. Generalized Gradient Approximation Made Simple. *Phys. Rev. Lett.* **1996**, *77*, 3865−3868.
(28) Heyd, J.; Scuseria, G. E.; Ernzerhof, M. Hybrid functionals based on a screened Coulomb potential. *J. Chem. Phys.* **2003**, *118*, 8207−8215.
(29) Nørskov, J. K.; Rossmeisl, J.; Logadottir, A.; Lindqvist, L.; Kitchin, J. R.; Bligaard, T.; Jonsson, H. Origin of the Overpotential for Oxygen Reduction at a Fuel-Cell Cathode. *J. Phys. Chem. B* **2004**, *108*, 17886−17892.

https://doi.org/10.1021/acs.chemmater.1c04167
Chem. Mater. 2022, 34, 4336−4343